

# THE ACCELERATION RELATION IN GALAXIES AND SCALE INVARIANT DYNAMICS: ANOTHER CHALLENGE FOR DARK MATTER

ANDRE MAEDER<sup>1</sup>

<sup>1</sup>*Geneva Observatory  
chemin des Maillettes, 51  
CH-1290 Sauverny, Switzerland*

(Received; Revised; Accepted)

Submitted to ApJ

## ABSTRACT

A relation between the centripetal acceleration  $g_{\text{obs}}$  in galaxies and the gravity due to the baryon distribution  $g_{\text{bar}}$  has been found by [McGaugh et al. \(2016\)](#) and [Lelli et al. \(2017\)](#). It also summarizes properties such as the Tully-Fisher and Faber-Jackson relations. Below about  $10^{-10} \text{ m s}^{-2}$ , the observed relation deviates from the 1:1 line,  $g_{\text{obs}}$  being much larger than  $g_{\text{bar}}$ . The acceleration relation is followed by late and early type galaxies, and also by the dwarf spheroidals where the deviations from the 1:1 line are the largest ones. These deviations are currently attributed to dark matter.

We show that the scale invariant theory, with the assumption of the scale invariance of the empty space, correctly predicts the observed deviations in the acceleration relation. The large deviations (up to a factor 400) and the flattening of the acceleration relation observed for the dwarf spheroidal galaxies are also well described. The presence of dark matter is no longer necessary in the scale invariant context, which also accounts why dark matter usually appears to dominate in galactic regions with low baryonic gravities.

*Keywords:* Cosmology: theory - dark matter - Galaxies: rotation.

## 1. INTRODUCTION: THE CONTEXT

A most remarkable relation between the radial acceleration traced by the rotation curves of galaxies and the acceleration expected from the observed distribution of baryons has been found by [McGaugh et al. \(2016\)](#) and [Lelli et al. \(2017\)](#). Their major conclusion is that the dark matter distribution is fully determined by that of the baryons. These authors state, as a basic rule, that when the baryonic distribution is measured, the rotation curve follows and vice-versa. Even the dwarf spheroidal galaxies (dSphs) that are heavily dark matter dominated, with ratios of the total vs. baryon mass between 10 and 1000, satisfy the above relation. According to [Lelli et al. \(2017\)](#), the acceleration relation suggests the need of "a revision of the standard dark matter paradigm". In fact, the new relation expresses in a clear and synthetic way an ensemble of observational facts that progressively emerged over the previous decades, see detailed references in [McGaugh et al. \(2016\)](#) and [Lelli et al. \(2017\)](#). As they show, the discovered relation also encompasses and generalizes several well known dynamical properties of galaxies, such as the Tully-Fisher and Faber-Jackson relations ([Tully & Fisher 1977](#); [Faber & Jackson 1976](#)).

New cosmological models have recently been proposed, which include the specific hypothesis that the macroscopic empty space is invariant to a scale transformation, a property absent from general relativity with a cosmological constant, but present in the Maxwell equations ([Maeder 2017a](#)). These models predict an accelerated cosmic expansion without advocating the existence of some unknown form of dark energy. Several comparisons between models and observations have been performed: on the distance vs. redshift relation, the  $m - z$  diagram, the  $\Omega_\Lambda$  vs.  $\Omega_m$  plot, the age vs.  $H_0$  relation, the expansion rate  $H(z)$  vs. redshift  $z$  relation and on the redshift of the transition from braking to cosmic acceleration. A critical analysis of the CMB temperatures as function of  $z$  from CO molecules in DLA is also supporting these models ([Maeder 2017b](#)).

The scale invariant models also have some consequences for weak gravitational fields. From the scale invariant geodesic equation, the relation corresponding to the Newton law is obtained. It contains an additional small outward acceleration term, which is particularly significant in low gravity and low density regions ([Maeder 2017c](#)). This leads to an energy relation, which in the case of clusters of galaxies provides mass determinations much smaller than usual, letting little or no room for dark matter. A detailed study of the two-body problem has also been made in the scale invariant framework. This allows, alike the MOND theory ([Milgrom 1983](#)), but in a more general context, to account for the flat rotation curve of the Milky Way and galaxies ([Sofue & Rubin 2001](#); [Sohn et al. 2017](#)), and also why no dark matter is observed in forming galaxies at redshifts around  $z = 2$  ([Wuyts et al. 2016](#); [Genzel et al. 2017](#); [Lang et al. 2017](#)).

Here, we want to check whether the relation found by [McGaugh et al. \(2016\)](#) and [Lelli et al. \(2017\)](#) can be interpreted within the scale invariant framework. Section 2 recalls the McGaugh and Lelli acceleration relation and its main properties. In Sect. 3, after some recalls and an additional demonstration of the gauging condition, the acceleration relation is studied in the scale invariant context. In Section 4, the observations and predictions of the scale invariant theory are compared. Section 5 presents a critical discussion about dark matter and on some possibilities to distinguish between different proposed theories. The conclusions are given in Section 6.

## 2. THE OBSERVATIONS AND THEIR ANALYSIS

### 2.1. The observations

The observations are based on the study of 240 galaxies with spatially resolved photometric and kinematic data ([Lelli et al. 2017](#)). The sample contains 153 late-type galaxies (LTGs), representing 2693 measurement points ([McGaugh et al. 2016](#)). The data come from near infrared Spitzer photometry, which traces the distribution of stellar mass, and from high quality 21 cm HI data for the rotation curves ([Lelli et al. 2016](#)). There are 25 early-type galaxies (ETGs), ellipticals and lenticulars with stellar and HI data from ATLAS<sup>3D</sup> ([Cappellari et al. 2013](#)) and Chandra X-ray data ([Buote & Humphrey 2012](#)). The sample also contains 62 dwarf spheroidal galaxies (dSphs), with data from high resolution spectroscopy.

For the LTGs, which are rotationally supported spiral and irregular galaxies, [McGaugh et al. \(2016\)](#) and [Lelli et al. \(2017\)](#) define a centripetal acceleration called  $g_{\text{obs}}(R)$  at galactocentric distance  $R$ ,

$$g_{\text{obs}}(R) = \frac{v_{\text{circ}}^2(R)}{R} = \left| \frac{\partial \Phi_{\text{tot}}}{\partial R} \right|, \quad (1)$$

where  $v_{\text{circ}}(R)$  is the circular velocity of the galaxy and  $\Phi$  the total potential at distance  $R$ . The values of  $v_{\text{circ}}(R)$  are obtained from the above mentioned velocity observations. From the observed radial density profiles of stars and

gas, the authors compute the local baryonic potential  $\Phi_{\text{bar}}(R)$  in the galactic plane by numerically solving the Poisson equation  $\nabla^2 \Phi_{\text{bar}} = 4\pi G \rho_{\text{bar}}$ . A typical galactic thickness is assumed. The local acceleration  $g_{\text{bar}}(R)$  due to the baryonic component is then derived by

$$g_{\text{bar}}(R) = \left| \frac{\partial \Phi_{\text{bar}}}{\partial R} \right|. \quad (2)$$

The two accelerations  $g_{\text{obs}}(R)$  and  $g_{\text{bar}}(R)$  result from independent measurements. In absence of dark matter, they should be equal. Fig. 1 shows the relation between  $g_{\text{obs}}(R)$  and  $g_{\text{bar}}(R)$  for LTGs from [McGaugh et al. \(2016\)](#) and [Lelli et al. \(2017\)](#). The correlations is remarkably tight despite the fact it concerns different parts of different galaxies. High mass, high density galaxies populate the high gravity parts of the distribution and vice-versa. The authors also show that the small residuals show no relations with the radii, surface densities or gas fractions. As they emphasize, the dark matter content is locally entirely determined by the baryons.

In the early-type galaxies (ETGs), the pressure support contributes more than rotation to the total velocity dispersion. In the inner regions, [Lelli et al. \(2017\)](#) use the Jeans anisotropic models of [Cappellari et al. \(2013\)](#) which fit the velocity dispersion map to get an estimate of the total acceleration. At large radii, the velocity field is directly observable from the analysis of HI data by [den Heijer et al. \(2015\)](#), thus providing an estimate of  $g_{\text{obs}}(R)$ . The baryonic accelerations are estimated from the surface brightness profiles. This concerns 16 ETGs which are mainly disk ellipticals and lenticulars. For the 9 remaining ETGs which are giant boxy ellipticals, the information from X-ray observations is used to derive the total acceleration. The analysis of the X-ray data provide both the density and temperature profiles, which may lead to the determination of the enclosed gravitational mass within a given radius and thus of the acceleration  $g_{\text{obs}}$  acting locally ([Buote & Humphrey 2012](#)). The baryon acceleration is derived from Spitzer surface photometry, with account of the hot gas contribution for the X-ray ETGs.

The dwarf spheroidal galaxies (dSphs) are essentially pressure supported, having no rotating disk. The velocity dispersions are based on high resolution spectroscopy from the literature. The references for 62 dSphs and their relevant data, in particular their distances, luminosities, deprojected half-light radii, ellipticities, mean velocity dispersions, numbers of stars used and estimates of  $g_{\text{obs}}(R)$  and  $g_{\text{bar}}(R)$  are given in Appendix B by [Lelli et al. \(2017\)](#). The total masses and thus  $g_{\text{obs}}$  at the half-light radius are estimated from the velocity dispersions, according to a method by [Wolf et al. \(2010\)](#) who derived an accurate mass estimator for dispersion-supported stellar systems such as globular clusters, dwarf and elliptical galaxies. The baryonic accelerations are estimated from the stellar V-luminosities. The "ultrafaint" spheroidals have been discovered over the last ten years. Their relevant data, which have sizable uncertainties, are also given by [Lelli et al. \(2017\)](#). To constrain the low acceleration part of the relation  $g_{\text{obs}}(R)$  vs.  $g_{\text{bar}}(R)$ , [Lelli et al. \(2017\)](#) have proceeded to a critical analysis of the data quality, retaining only the objects with a sufficient number of velocity measurements, low ellipticity and limited tidal interaction with their host galaxy.

## 2.2. Some properties of the complete sample

The complete sample of 240 galaxies ([Lelli et al. 2017](#)) represents a few thousands of individual measurement points. The LTGs dominate the sample and their results are shown in Fig. 1. In this plot, the low mass galaxies ( $M < 3 \cdot 10^{10} M_{\odot}$ ) occupy the lower part of the curve, while the high mass galaxies cover almost the whole range. Fig. 1 implies that for low-mass, low-surface-brightness galaxies, some dark matter is already present in their deep interiors and it still increases with radii. For high-mass, high-surface-brightness galaxies, the inner part is fully baryon dominated (the curve coincides with the 1:1 line) while the outer layers are dark matter dominated. There is an overlap of the outer layers of massive galaxies and the small mass galaxies.

For the LTGs, the authors have explored the various possible correlations of the centripetal acceleration  $g_{\text{obs}}(R)$  with different galactic parameters: the gravity from baryons  $g_{\text{bar}}$ , the stellar gravitational field, the total surface stellar density (bulge + disk) and the disk stellar density. They found that the most fundamental relation is that with the gravitational potential  $g_{\text{bar}}(R)$  rather than with the local density.

The different types of galaxies preferentially occupy different parts of the curve, with also some large overlaps. The LTGs are mainly in the range between  $g_{\text{bar}} = 10^{-9.5}$  and  $10^{-11.5} \text{ m s}^{-2}$ . The ETGs are distributed toward the high accelerations, between  $10^{-8}$  down to about  $10^{-11} \text{ m s}^{-2}$ . Finally, the dSphs occupy the range below  $10^{-11}$  down to about  $10^{-12.5} \text{ m s}^{-2}$ , while the ultrafaint dSphs extend the relation from about  $10^{-12}$  to  $10^{-13.5} \text{ m s}^{-2}$ .

The ETGs follow the same relation as the LTGs, independently whether they are X-ray emitters or not. The inner parts of ETGs have a negligible dark matter content, while the outer layers present significant excesses. Unlike the LTGs and ETGs, the dSphs are represented only by one point per galaxy. The classical dSphs are located on the same

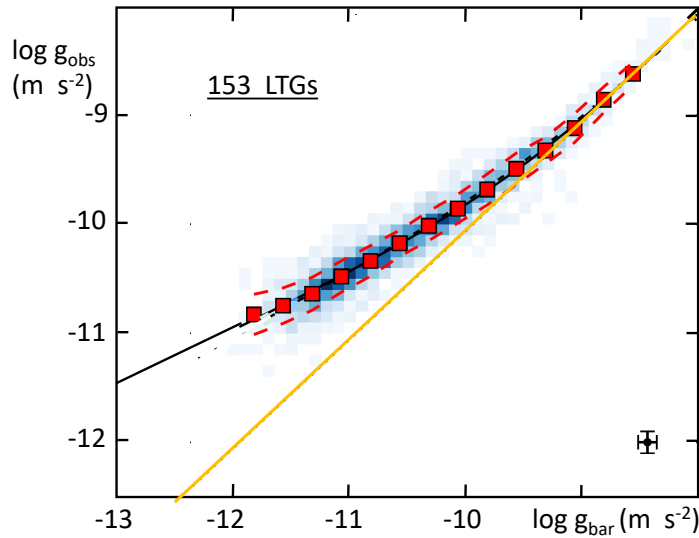


**Figure 1.** The centripetal acceleration  $g_{\text{obs}}(R)$  versus the baryonic acceleration  $g_{\text{bar}}(R)$  for binned data from 2693 measurement points of 153 LTGs by [McGaugh et al. \(2016\)](#), see also Fig. 3 by [Lelli et al. \(2017\)](#). The continuous line is an average fitting by McGaugh et al., the average error bar on the binned points is indicated in the lower right corner. The yellow line shows the line where the two accelerations would be equal.

relation as the LTGs, in the location of the outer parts of the high-mass galaxies. The extreme of them, the ultrafaint dSphs, show a marked flattening of the acceleration curve (see Fig. 2 -5). These results agree with the picture that the ultrafaint dSphs are the most dark-matter-dominated galaxies, with some objects having a mass-luminosity ratio up to  $\sim 1000$  ([Strigari et al. 2008](#)). This raises the question why the dSphs contain so much dark matter, a question without an answer.

The fact that there is an excellent continuity in the average curve delineated by the different types of galaxies is a remarkable property. This is especially noticeable for a sample of galaxies covering a range of nearly 4 dex in galactic masses, and containing both rotationally and pressure supported galaxies. This strengthens the view by [McGaugh et al. \(2016\)](#) and [Lelli et al. \(2017\)](#) that the above relation expresses a fundamental property of galaxies: the observed baryon distribution determines the velocity distribution.

### 3. THE RELATION BETWEEN THE GRAVITIES IN THE SCALE INVARIANT THEORY

#### 3.1. The gauging conditions

Developments in the scale invariant theory of gravitation have been made by [Weyl \(1923\)](#), [Eddington \(1923\)](#), [Dirac \(1973\)](#) and [Canuto et al. \(1977\)](#). The mathematical context is that of the cotensor calculus, which in addition to the general covariance also considers scale changes. A scale transformation of the line element  $ds'$  of general relativity is expressed by  $ds' = \lambda(x^\mu)ds$ , where  $ds$  is a new line element. There,  $\lambda$  is the scale factor, which for reasons of homogeneity and isotropy only depends on time. Scale covariant derivatives, modified Christoffel symbols, the Riemann-Christoffel tensor also have their scale covariant expressions. A general scale covariant field equation can be written ([Canuto et al. 1977](#)), it contains some functions of  $\lambda$  and its first two derivatives, it also contains the cosmological constant, often discussed in this context ([Cervero & Estevez 1982](#)).

To solve the resulting system of equations, we need to have some additional constraint on  $\lambda(t)$ . The hypothesis we have introduced ([Maeder 2017a](#)) is that the macroscopic empty space is invariant to a scale transformation of the above form. The Minkowski metric is then applied to the empty space, after we have examined at which condition it can be done, see Equation (17) in [Maeder \(2017a\)](#). As a result, we obtain two differential relations between the scale factor  $\lambda(t)$ , its derivatives and the cosmological constant  $\Lambda_E$ ,

$$3 \frac{\dot{\lambda}^2}{\lambda^2} = \lambda^2 \Lambda_E, \quad (3)$$

$$\frac{\ddot{\lambda}}{\lambda} = 2 \frac{\dot{\lambda}^2}{\lambda^2}, \quad (4)$$

or some combination of the two. The solution of these equations gives  $\lambda$  varying like  $1/t$ . Thanks to these relations  $\Lambda_E$  can be eliminated from the cosmological equations and a fully determined system of equations is obtained for the chosen metric. Interestingly enough, the above relations also bring major simplifications to the cosmological equations.

Now, we examine an independent way to establish a relation between the cosmological constant  $\Lambda_E$  and the scale factor. The cosmological constant is related by some constant factor to the energy density  $\varrho_v$  of the empty space, see for example [Carroll et al. \(1992\)](#),

$$\Lambda_E = 8\pi G \varrho_v, \quad (5)$$

with  $c = 1$ . Let  $\ell'$  be a constant line element in the space of general relativity. In the scale covariant space, the line element becomes  $\ell = \frac{\ell'}{\lambda(t)}$ , where  $\lambda$  may only be a function of the cosmic time  $t$  as said above. The possible variations of the scale factor  $\lambda$  will contribute to the energy density present in the empty space. Thus, if  $\lambda(t)$  varies, the energy density present in the empty space will depend on

$$\dot{\ell}^2 = \ell'^2 \frac{\dot{\lambda}^2}{\lambda^4}. \quad (6)$$

If there is no other source of energy in the macroscopic empty space, for a constant value of  $\lambda(t)$  the energy density of the empty space and thus  $\Lambda_E$  are both equal to zero. The cosmological constant according to Equation (5) is proportional to  $\dot{\ell}^2$ ,

$$\Lambda_E = \text{const.} \frac{\dot{\lambda}^2}{\lambda^4}, \quad (7)$$

which compares with Equation (3). The cosmological constant  $\Lambda_E$  is a true constant and this implies,

$$\frac{d\Lambda_E}{dt} = 0 \quad \implies \quad \frac{d\dot{\ell}^2}{dt^2} = 2\dot{\ell}\ddot{\ell} = \ell'^2 \left( \frac{\ddot{\lambda}}{\lambda^4} - 2\frac{\dot{\lambda}^3}{\lambda^5} \right) = 0. \quad (8)$$

Expressing  $\ddot{\ell}$ , we get

$$\ddot{\ell} = \frac{\ell'}{\lambda} \left( \frac{\ddot{\lambda}}{\lambda} - 2\frac{\dot{\lambda}^2}{\lambda^2} \right). \quad (9)$$

The second derivative of  $\ell$  should be zero in order to satisfy Equation (8) for  $\dot{\ell} \neq 0$ , thus

$$\ddot{\ell} = 0, \quad \implies \quad \frac{\ddot{\lambda}}{\lambda} = 2\frac{\dot{\lambda}^2}{\lambda^2}, \quad (10)$$

in agreement with Equation (4). We see that the gauging conditions, independently obtained 1) from the application of Minkowski metric to the scale invariant empty space and from 2) the properties of the energy density of the empty space associated to the gauge variations, are both giving identical results. This confirms the consistency of the adopted gauging condition. In general relativity, the cosmological constant and thus the density of the empty space is independent of the material content of the Universe, similarly this also applies to the conditions (3) and (4) expressing the cosmological constant in terms of the scale factor of the empty space. We also see that the only significant energy in the large scale empty space is that resulting from the gauge variations. Indeed, this is the case, even if this is not necessarily true at the quantum level, in the same way as we may use Einstein theory at large scales, even if we cannot do it at the quantum level.

With the Robertson-Walker metric, the above gauging conditions (3) and (4) enable us to express the cosmological equations (29) - (31) in [Maeder \(2017a\)](#). The resulting models predict an acceleration of the cosmic expansion and satisfy various cosmological tests.

### 3.2. Some basic useful relations in the scale invariant context

The equation of geodesics in the scale invariant context ([Dirac 1973](#); [Canuto et al. 1977](#)) was shown to be consistent with the usual definition of geodesics, as the line of shortest distance between two points [Bouvier & Maeder \(1978\)](#). A demonstration of the geodesic equation is also given with an application to the weak field approximation leading to a modified Newton equation ([Maeder & Bouvier 1979](#); [Maeder 2017c](#)). In addition to the usual gravitational attraction

it contains a small outward acceleration, particularly significant in low gravity and low density media. The equation writes

$$\frac{d^2 \mathbf{r}}{dt^2} = -\frac{GM}{r^2} \frac{\mathbf{r}}{r} + \kappa(t) \frac{d\mathbf{r}}{dt}, \quad (11)$$

where  $\kappa(t) = 1/t$  with  $t$  being the cosmic time. The additional term results from the cosmological constant, which itself depends on  $\lambda$  by Equation (3) so that the additional term is determined by  $\lambda$  and its first derivative. For a constant scale factor  $\lambda$ , there is no outward acceleration term. For a range of low gravities, the present predictions and that of the MOND theory (Milgrom 1983, 2009) may be rather similar, however the basic equations and predictions are not the same and there are possibilities to distinguish between the two theories, see also Section (5.3). The law of conservation of angular momentum  $L$  is different from the usual one,

$$\kappa(t) r^2 \dot{\vartheta} = L = \text{const.} \quad (12)$$

It is a scale invariant quantity. The equation of motion (11) has been applied to the two-body problem and an equivalent form to Binet equation has been found. The orbits  $r(\vartheta)$  belong to the usual family of conics, with in addition a slight outward expansion motion,

$$r = \frac{r_0}{1 + e \cos(\vartheta)}, \quad \text{with} \quad r_0 = \frac{L^2}{GM \kappa^2(t)}, \quad (13)$$

where  $r_0$  is the radius of the circular orbit. The eccentricity  $e$  is scale invariant, while  $r_0$  varies like  $t$ . The circular velocity in the case of the two-body problem is according to Equation (12)  $v_{\text{circ}} = r_0 \dot{\vartheta} = \frac{L}{\kappa(t) r_0}$ , which is also a scale invariant quantity. Now, with the expression (13) for  $r_0$ , one obtains

$$v_{\text{circ}}^2 = \frac{GM \kappa(t)}{L} = \frac{GM}{r_0}. \quad (14)$$

The expression relating the circular velocity and the gravitational potential is valid. Consistently, the gravitational potential is also a scale invariant quantity, since we have both  $r' = \lambda r$  and  $M' = \lambda M$ , as already seen in Maeder (2017a). For an elliptical motion, the semi-major axis  $a$  and the period  $P$  also behave like  $\dot{a}/a = \dot{P}/P = 1/t$ . These relations illustrate the main properties of the motions. The additional outward acceleration term in Equation (11) does not produce a change of the circular velocity, but just an extension of the orbit and a corresponding reduction of the angular velocity.

### 3.3. Relation between the "observed and baryonic" gravities

We need a relation between the gravities  $g_{\text{obs}}$  and  $g_{\text{bar}}$ , as defined by McGaugh et al. (2016) and Lelli et al. (2017). A gravitational system governed by Equation (11) never reaches a state of equilibrium and the additional term in this equation does not derive from a potential, thus the conditions are different from those of the usual virial theorem. However, we may find an expression which relates the different forms of energy present. Let us consider the ensemble of  $N$  stars moving in a galaxy. According to Eq.(11), the acceleration of a star  $i$  interacting with another one of mass  $m_j$  is

$$\frac{dv_{ij}}{dt} = -\frac{Gm_j}{r_{ij}^2} + \kappa(t) v_{ij}, \quad (15)$$

where  $r_{ij}$  is the distance between objects  $i$  and  $j$  and  $v_{ij} = \frac{dr_{ij}}{dt}$ . First, we multiply this equation by  $v_{ij}$  and get

$$\frac{1}{2} d(v_{ij}^2) = -\frac{Gm_j}{r_{ij}^2} dr_{ij} + \kappa(t) v_{ij}^2 dt, \quad (16)$$

We now call  $v_i$  the velocity of the star  $i$  due to its interactions with all the  $N$  other ones,

$$\frac{1}{2} d(v_i^2) = -\frac{1}{N} \sum_{j \neq i} \frac{Gm_j}{r_{ij}^2} dr_{ij} + \kappa(t) v_i^2 dt, \quad (17)$$

where  $v_i^2 = \frac{1}{N} \sum_{j \neq i} v_{ij}^2$ . Now, we take the mean of the above relation over all the  $N$  stars,

$$\frac{1}{2N} \sum_i d(v_i^2) = -\frac{1}{2N^2} \sum_i \sum_{j \neq i} \frac{Gm_j}{r_{ij}^2} dr_{ij} + \frac{1}{N} \sum_i \kappa(t) v_i^2 dt. \quad (18)$$



We have  $\overline{v^2} = \frac{1}{N} \sum_i v_i^2$ . The double summation on the right represents a total of  $N(N-1)/2$  individual interactions between the stars in the galaxy. Thus, the division of the double summation by  $1/(2N^2)$  expresses the average gravitational interaction of a star with the ensemble of the stars in the system, ( $N-1$  is taken equal to  $N$ , since  $N$  is very large). The factor  $1/2$  in front of the first term on the right is evidently necessary in order not to count twice each gravitational interaction. (We note that the term  $\frac{G m_j}{r_{ij}^2} dr_{ij}$  is scale invariant since the effects of a change of scale act the same way on masses and radii, even if the distances  $r_{ij}$  vary as a result of particular motions.) From what precedes, we may write,

$$d(\overline{v^2}) \approx -q' \frac{GM}{R^2} dR + 2 \kappa(t) \overline{v^2} dt, \quad (19)$$

where  $M$  and  $R$  are the total mass and radius of the considered gravitational configuration and  $q'$  a structural factor, all at the time considered. The above expression has to be integrated between times  $t_{\text{in}}$ , the time of the galaxy formation and the present time  $t_0$ . (The analyzed galaxies of the present sample have small redshifts and thus it is like if they are observed at the present time.) At time  $t_{\text{in}}$ , the time of their rapid formation, we consider that the effects resulting from the left term and the first term on the right of Equation (19) are in equilibrium. As above, the gravitational potential  $GM/R$  is a scale invariant quantity and thus it does not vary over the ages. With account of these remarks, after integration we get the following energy equation,

$$\overline{v^2} \approx q \frac{GM}{R} + 2 \int_{t_{\text{in}}}^{t_0} \kappa(t) \overline{v^2(t)} dt. \quad (20)$$

The first two terms in this equation are identical to those of the classical virial theorem. We see that in addition we have on the right side the cumulative contribution of the additional term over the ages. The structural factor  $q$  could be slightly different from  $q'$  due to the evolution of the system. In the standard case,  $q = 3/5$  for a constant spherical distribution, for a constant disk  $q = 2/3$ . The values  $M$  and  $R$  can be taken as the present values of mass and radius of the system. The velocities  $v$  refer to the total velocities.

Let us express the above equation as a function of the variables used by [McGaugh et al. \(2016\)](#) and [Lelli et al. \(2017\)](#), in particular of the gravities they consider. For this purpose, the following approximation is made,

$$2F \equiv 2 \int_{t_{\text{in}}}^{t_0} \kappa(t) \overline{v^2(t)} dt \approx 2f \frac{\overline{v^2}}{t_0} \Delta t, \quad (21)$$

where  $f$  accounts for the fact that the mean of  $\frac{v^2}{t}$  over the galaxy lifetime  $\Delta t$  should be taken. The factor  $f$  is of the order of unity, (in Sect. 4.2 we examine the effects of different values of  $f$  and other parameters). The interval of time  $\Delta t$  is equal to the total distance  $\Delta r$  covered by a typical star during its circular motions around the center of a galaxy at a constant circular velocity  $\overline{v_{\text{circ}}}$ , thus  $\Delta t \approx \Delta r / \overline{v_{\text{circ}}}$ . The total distance  $\Delta r$  is given by the number  $n$  of circular orbits that a representative star has described during its lifetime, thus  $\Delta r \approx n \times 2\pi \overline{R}$ , where  $\overline{R}$  is a time average of the typical radius during the galaxy lifetime. For example, for a star like the Sun at 8 kpc from the galactic center with a circular velocity of 240 km/s, one galactic orbit represents about  $2.05 \times 10^8$  yr. This value would lead to  $n \approx 49$  in 10 Gyr and to  $\log g_{\text{obs}} = -9.63$ . The values of  $n$  may be of the order of a few tens, however the possible range of radii and velocities is rather large (see Sect. 4.2).

From Equation (2), the circular velocity is  $v_{\text{circ}} = (g_{\text{obs}} R)^{1/2}$ . According to Equation (14), the circular velocity is an invariant, thus its value at the present time may be considered. For the relation between the time average and present radius, the approximation  $\overline{R} \approx (1/2)R$  is taken, in this respect we note that any deviation from the  $1/2$  factor can be easily included in the value of " $f$ ". This leads to

$$2F \approx 2f \frac{\overline{v^2}}{t_0} \frac{2\pi n \overline{R}}{(g_{\text{obs}} R)^{1/2}} \approx 2f \frac{\overline{v^2}}{t_0} n\pi \left( \frac{R}{g_{\text{obs}}} \right)^{\frac{1}{2}}. \quad (22)$$

The energy equation (20) then becomes

$$\overline{v^2} \left[ 1 - \frac{2fn\pi}{t_0} \left( \frac{R}{g_{\text{obs}}} \right)^{\frac{1}{2}} \right] \approx q' \frac{GM}{R}. \quad (23)$$

As a matter of fact, the observed velocities are obtained by some projections of the total velocities, thus the estimates of  $g_{\text{obs}}$  are based on  $\overline{v^2}/R$ . The mean gravitational acceleration  $\frac{GM}{R^2}$  is identified with  $g_{\text{bar}}$ , so that the relation connecting

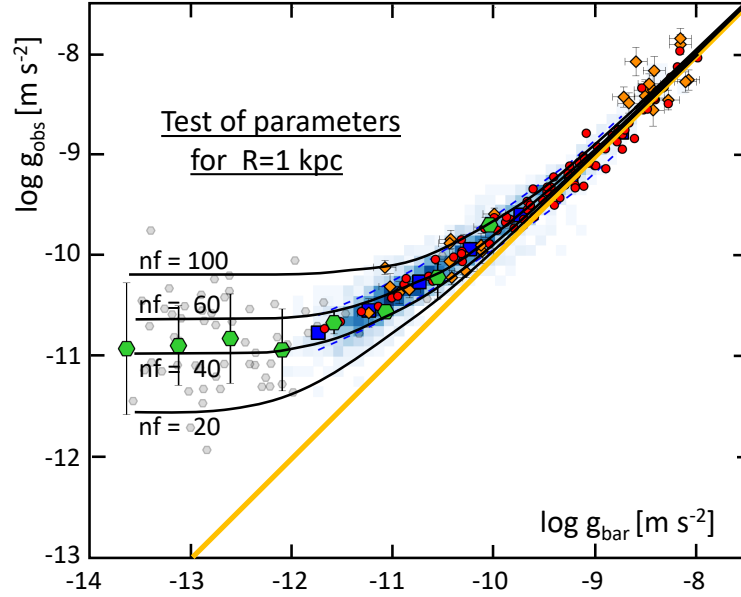


**Figure 2.** The acceleration relation for all galaxies studied by Lelli et al. (2017) according to their Fig. 12 left, with superimposed continuous black lines derived from Equation (24) for different values of the product  $nf$ ,  $q'$  is taken equal to unity. A reference value of  $R = 1$  kpc is taken. The blue squares represent the binned data for 153 LTGs, the thin blue broken lines indicate the standard deviation around their average. The rotating ETGs are represented by red circles, and the X-ray ETGs by orange diamonds. The small grey hexagons show the dwarf spheroidals, while the large green hexagons give their mean values. Vertical and horizontal bars show standard deviations. The yellow line shows the relation where the two gravities are equal.

the two gravities may be written,

$$g_{\text{obs}} \left[ 1 - \frac{2fn\pi}{t_0} \left( \frac{R}{g_{\text{obs}}} \right)^{\frac{1}{2}} \right] \approx q' g_{\text{bar}}. \quad (24)$$

This relation contains several approximations and uncertain numerical coefficients, it nevertheless expresses the main relation between the two gravities  $g_{\text{obs}}$  and  $g_{\text{bar}}$ , as expected from the effects of the scale invariant dynamics considered in this work. In the quantitative comparisons below, we shall examine the main uncertainties due to the factors  $n$  and  $f$ . The above expression indicates that for a given  $g_{\text{bar}}$  the corresponding  $g_{\text{obs}}$  may be larger. The lower the gravities of the considered galaxies, the larger will be the differences between  $g_{\text{obs}}$  and  $g_{\text{bar}}$ . This is the origin of the upward deviations from the 1:1-line in a plot like Fig. 1.

#### 4. COMPARISONS BETWEEN MODELS AND OBSERVATIONS

##### 4.1. The range of parameters of the observed galaxies

Let us examine the parameters intervening in Equation (24). The distances of LTGs in the SPARC sample (Lelli et al. 2016) are within the range of a few tens of Mpc. The same for the ETGs (den Heijer et al. 2015). The spheroidals, except one, are closer than 1 Mpc (Lelli et al. 2017). Thus, it is appropriate to consider that all the galaxies in the sample are observed at the present time  $t_0$ .

For the LTGs, Lelli et al. (2017) consider various definitions of the radius. The effective radii  $R_{\text{eff}}$  encompass the half of the luminosities, they range from about 0.5 kpc to 15 kpc. The radii  $R_s$  give the scale length of the stellar disk, they cover the same range as  $R_{\text{eff}}$ . The radii  $R_{\text{HI}}$  indicate the distances where the surface HI density reaches  $1 M_{\odot} \text{ pc}^{-2}$ . They cover a much larger range than the previous radii, going from about 2 kpc to 60 kpc. For the ETGs, the HI radii also range from a few kpc to tens of kpc (den Heijer et al. 2015). At the other extreme, the spheroidal galaxies have radii around 1 kpc for the richest ones, with values down to about 0.1 kpc for the smallest ones. The average size of the dSphs fulfilling the quality criteria defined by Lelli et al. (2017) is 530 pc.

##### 4.2. Comparisons for different values of $nf$ and $R(\text{kpc})$



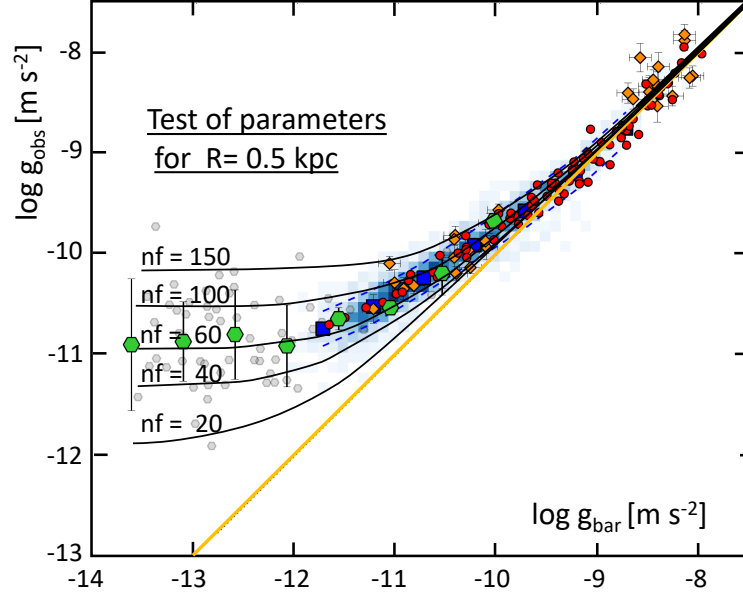


**Figure 3.** The same as Fig. 2 with a reference radius of 0.5 kpc.

The complete sample of 240 galaxies has been represented by Lelli et al. (2017) in their Fig. 12 left, this figure is used as the basis for comparisons with the predictions of Equation (24). With respect to Fig. 1, the data for ETGs confirm those for LTGS, while the dSphs extend the curve to the left with a distinct flattening for the lowest gravities, in particular for the ultrafaint spheroidals.

We want first to estimate the product  $nf$  of the parameters  $n$  and  $f$ . Curves for a radius  $R = 1$  kpc with values  $nf = 20, 40, 60$  and  $100$  are shown in Fig. 2. For the high gravities, all the curves are close to the 1:1 yellow line and thus the main constraint comes from the low gravity objects which show the largest deviations, in particular the spheroidal galaxies. A value of  $nf$  between 40 and 60 well corresponds to the mean data over the all range, the large deviations of the spheroidals, which represent the main constraint, are well reproduced. This range of  $nf$  makes some sense as seen above. In Fig. 3, the same kind of plot is made for different values of  $nf$ , but for a reference radius  $R = 0.5$  kpc corresponding to the mean of dwarf spheroidals as given above. We see that the curve with  $nf = 60$  reproduces the mean of the distribution of the spheroidal galaxies as well as for the ETGs and LTGs.

Fig. 4 shows the curves derived from relation (24) for different values of the radii  $R = 0.2, 0.5, 1, 2, 5$  and  $10$  kpc for a parameter  $nf = 40$ . We notice that the curves for  $R = 1$  and  $2$  kpc well encompass the observed points for the galaxies or parts of galaxies with low gravities. These are mainly low mass spirals, or external parts of massive spirals and spheroidals. The means of dSphs represented by the large green points is also around  $R = 1$  to  $2$  kpc, which is slightly too large and may favor a slightly higher  $nf$  value. However, the remarkable fact is that the general curve and the flattening for low gravities is well reproduced. This flattening results from the fact that for lower values of  $g_{\text{obs}}$  the parenthesis in Equation (24) tends to zero, and to  $-\infty$  in log scale. This appears as the reason for the flattening of the curves for the lowest baryonic gravities, where the predicted curves tend toward a horizontal asymptotic line, in agreement with the general trend discovered by McGaugh et al. (2016) and Lelli et al. (2017). Fig. 5 shows the same kind of figure for a reference value  $nf = 60$ , which as seen above gives an excellent fit for  $R = 0.5$  kpc. The smallest spheroidals are below the line for  $R = 0.2$  kpc, while they are absent in the region corresponding to large radii. For large LTGs and ETGs, the curves corresponding to different radii are all rather close to the 1:1 line, largely within the scatter of the data.

Indeed, both the parameters  $R$  and  $nf$  may vary along the observed curve from the highest to the lowest gravities. This is clearly the case for the radii, which range from tens of kpc for LTGs and ETGs down to about 0.1 kpc for the smallest ultrafaint spheroidals. What about  $nf$  and the orbital period? Above, we have seen that a star like the Sun at  $R = 8$  kpc, with  $v_{\text{circ}} = 240$  km/s and  $\log g_{\text{obs}} = -9.4$ , describes its circular orbit in about  $2.05 \cdot 10^8$  Gyr, thus making  $n = 49$  tours in 10 Gyr. A dwarf spheroidal galaxy has a much smaller typical radius  $R$ , but at the same time its velocity estimate based on the observed velocity dispersion is also much smaller, so that the corresponding

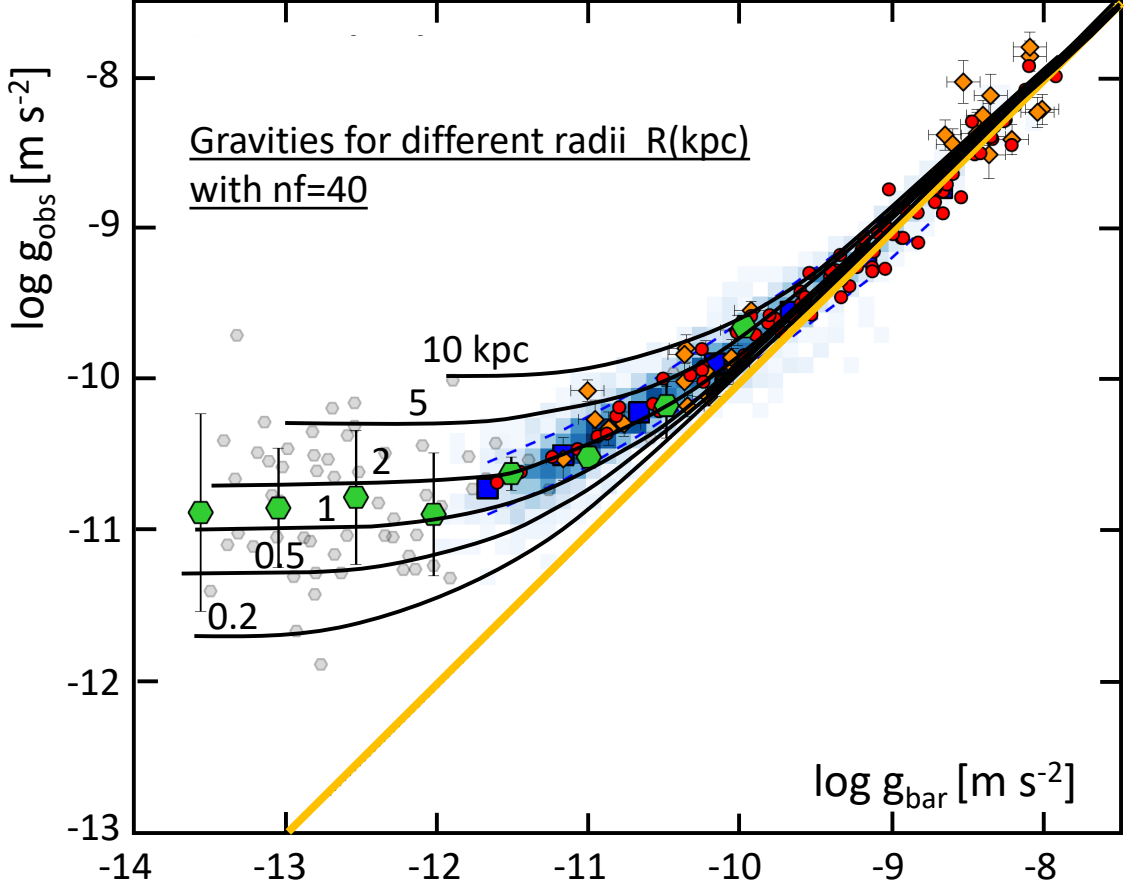


**Figure 4.** The acceleration relation for all galaxies studied by [Lelli et al. \(2017\)](#) according to their Fig. 12 left, with superimposed continuous black lines derived from Equation (24) for different values of the mean radii  $R(kpc)$ . A reference value of  $nf = 40$  is taken. Same remarks as for Fig. 2.

characteristic time is not so much different from the above one and thus the same for the corresponding  $nf$ -value. As an example, for a dwarf spheroidal with  $R = 0.5$  kpc and a value  $\log g_{obs} = -10.85$  (see Figs. 2–5), the corresponding velocity-value  $(g_{obs} \times R)^{\frac{1}{2}}$  would be 14.8 km/s, which in turn would correspond to an orbital period of  $2.08 \cdot 10^8$  Gyr similar to the above one and the same for  $nf$ . This high coincidence is accidental, but it nevertheless suggests that a given value of  $nf$  may relatively well describe some range of gravities. The reason is that the rotation velocity and the velocity dispersion are generally larger for larger galaxies.

Thus, the best curve to describe the observations in Fig. 5 is that with  $nf = 60$  on the flat part of the track with  $R=0.5$  kpc below  $g_{bar} \approx 10^{-11.5}$ , then it would become close to the curve for  $R = 2$  kpc near  $g_{bar} = 10^{-10}$  m s $^{-2}$ , then close to curves for  $R = 5$  kpc, 10 kpc, ... for higher gravities. At the same time, for higher gravities all curves are squeezed together near the 1:1 line and thus different  $nf$  or  $R$  values make only negligible differences.

On the whole, we conclude that Equation (24), despite its simple expression, well reproduces the main trends of the fundamental acceleration relation discovered by [McGaugh et al. \(2016\)](#) and [Lelli et al. \(2017\)](#). This supports the view that the cumulative effects of the additional term predicted by the above scale invariant developments may be at work in galaxies.

## 5. DISCUSSION

Several observed properties of galaxies are direct consequences of the acceleration relation found by [McGaugh et al. \(2016\)](#) and [Lelli et al. \(2017\)](#) and are thus consistent with the predictions of the scale invariant theory. We also discuss the dark matter problem and the way to distinguish between theories.

### 5.1. The Tully-Fisher, Faber-Jackson relations and other properties

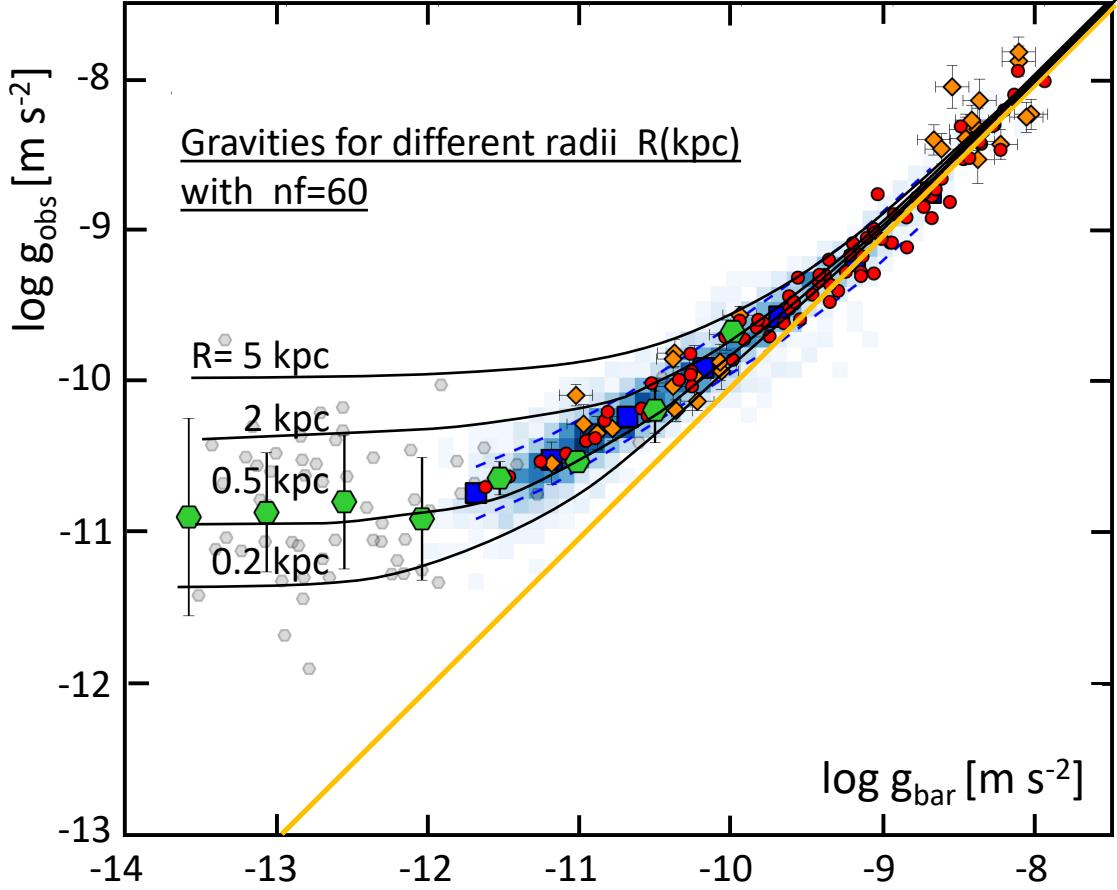


**Figure 5.** Same as Fig. 4 for a reference value of  $nf = 60$ .

The original Tully-Fisher relation (Tully & Fisher 1977) relates the luminosity of spiral galaxies to the velocity in the flat part of the rotation curve. Further works by McGaugh et al. (2000) demonstrate that there is also a well defined relation between the rotation velocity  $V$  in the flat part of the rotation curve and the baryonic mass  $M_{\text{bar}}$  of the form  $M_{\text{bar}} \sim V^4$ , this relation is the so-called BTFR. As pointed out by Lelli et al. (2017), the BTFR directly results from the fact that over a large part the observed acceleration relation does not follow the 1:1 line, but rather behaves more or less like  $g_{\text{obs}} \sim g_{\text{bar}}^{1/2}$  (see curve Fig 1). This implies that  $V^2 \sim M_{\text{bar}}^{1/2}$ , which gives a behavior of the baryonic mass with about  $V^4$ . As a consequence, the above relation (24) giving the acceleration relation is also implying the Tully-Fisher relation.

The Faber-Jackson relation (Faber & Jackson 1976) relates the luminosity (or the stellar mass) of the elliptical galaxies to their velocity dispersion  $\sigma$ . As shown by Lelli et al. (2017), the facts that 1) the velocity dispersion and the rotation velocities of rotating ellipticals are linearly related, and 2) that the rotating ETGs follow the same  $M_{\text{bar}} \sim V^4$  relation as the LTGs (den Heijer et al. 2015) lead to a relation of the form  $M_{\text{bar}} \sim \sigma^4$ . Thus, as for the BTFR, relation (24) implies the Faber-Jackson relation.

There is also a close correspondence between features in the luminosity profiles and in the rotation curves of galaxies. As quoted by Lelli et al. (2017), this property is known as "the Renzo rule" following Sancisi (2004), who emphasizes that "for any feature in the luminosity profile there is a corresponding feature in the rotation curve, and vice versa". These various facts, that are consequences of the acceleration relation, are all finding a consistent interpretation in the scale invariant context.

### 5.2. The interpretation in terms of dark matter

In the above figures 1 to 5, the vertical distance of the observed points above the yellow 1:1 line expresses the ratio of the dynamical (or total) masses  $M_{\text{dyn}}$  to the visible baryonic masses  $M_{\text{bar}}$ . One has thus the correspondence

$M_{\text{dyn}}/M_{\text{bar}} \approx g_{\text{obs}}/g_{\text{bar}}$  (Lelli et al. 2017). Interpreting the deviations as due to dark matter with mass  $M_{\text{DM}} = M_{\text{dyn}} - M_{\text{bar}}$ , one has for the mass in the form of dark matter,

$$M_{\text{DM}} \approx \left( \frac{g_{\text{obs}}}{g_{\text{bar}}} - 1 \right) M_{\text{bar}}. \quad (25)$$

The observations have shown that the parenthesis is a function of  $g_{\text{bar}}$  only and thus the assumed amount of dark matter is fully determined by the baryon properties or the reverse, as stated by (Lelli et al. 2017). For LTGs and ETGs, the ratio of dark to baryonic matter may reach a factor of 10, while for dwarf spheroidals it ranges from ten to about 400, with an extreme value up to about 1000. What is the process at the origin of such dark matter dominated objects? How can the baryonic component, that only represents 2-3 thousands of the total mass, determine everything? Another major source of astonishment about dark matter is the following one. *Since dark matter is participating to gravitational interactions, why is it generally more concentrated in low gravity regions, as indicated by the acceleration relation?*

We note that Equation (24) well explains why dark matter is relatively more abundant in low gravity regions and why the dwarf spheroidals are so extreme. The deviations from the 1:1 line negatively depend on the ratio  $(\frac{R}{g_{\text{obs}}})^{\frac{1}{2}}$ . Over the whole sample,  $g_{\text{obs}}$  varies by a factor  $10^3$ , while the half light radii cover a smaller range from 0.5 kpc for the average of dSphs to about 15 kpc. Thus, the variations of gravities dominate over the variations of radii, and, despite their smaller radii, the dwarf spheroidals have the largest term  $(\frac{R}{g_{\text{obs}}})^{\frac{1}{2}}$  in Equation (24).

### 5.3. Differences between theoretical predictions: the cumulative effects in time

Despite the large variety of galaxies studied, their differences in type, mass, radius, dynamical property, gas content, star formation rate, chemistry, etc., they all follow the acceleration relation. This illustrates the deep meaning of this relation which suggests a revision of our concepts about dark matter, as emphasized by Lelli et al. (2017). There are various possibilities, such as the hypotheses made about different kinds of unknown particles (Bertone & Hooper 2017; de Swart et al. 2017) or such as modifications of the gravity law as suggested here and in the MOND theory (Milgrom 1983, 2009).

The observational predictions of the scale invariant theory are well defined, which is not the case for many of the non-standard theories. The predictions concern for now several classical cosmological tests and a few dynamical tests about galaxies and clusters of galaxies. In all cases, agreement with observations was found. A particular signature, apparently specific to the scale invariant theory, resides in the cumulative effects in time, which for example lead to the increase of the velocity dispersion with aging. This is a dynamical effect typically observed for the "vertical" velocity dispersion of stars in the Milky Way, which expresses the vertical support perpendicular to the galactic plane (Maeder 2017c). Also, the velocities in external regions of galaxies appear to be relatively higher at present than in the past (Wuyts et al. 2016; Genzel et al. 2017; Lang et al. 2017).

Thus, a new prediction of the scale invariant theory is that the acceleration relation, derived from observed velocities, would less deviate from the 1:1 line for galaxies with higher redshifts  $z$ . In fact, the deviations would be present, but they would occur at even lower gravities for higher redshifts. Such properties, if consistently analyzed, may provide tests in order to discriminate between different non-standard theories.

## 6. CONCLUSIONS

The further study made about the gauging condition in Sect. 3.1 confirms the relation found earlier between the cosmological constant  $\Lambda_E$  and the scale factor  $\lambda(t)$ . The scale invariant equation of motion is applied to the study of the internal support in galaxies. It leads to a relation between the centripetal acceleration  $g_{\text{obs}}$  and the baryonic acceleration  $g_{\text{bar}}$  which deviates from the 1:1 relation below about  $g_{\text{bar}} = 10^{-10} \text{ m s}^{-2}$ . This corresponds to the observational results by McGaugh et al. (2016) and Lelli et al. (2017) based on 240 galaxies of different types.

We emphasized above that it is strange that the supposed dark matter, which experiences gravitational interactions, is precisely concentrating with large excesses, in the regions with lower gravities. In the scale invariant context, there is no need of dark matter to account for the observed acceleration relation. This is in agreement with previous results (Maeder 2017c) on the dynamical masses of clusters of galaxies, on the rotation velocities of galaxies and on the "vertical" velocity dispersion of stars in the Milky way. For now, we have no proof of the theory, however, the accumulation of positive results encourage the author to pursue further exploration.

I express my best thanks to D. Gachet for his support and to V. Gueorguiev for his support and useful comments.

## REFERENCES

- Bertone, G., Hooper, D. 2017, Dark-matter history, CERN Courier, 57, vol. 4, 27
- Bouvier, P., Maeder, A. 1978, *Astrophys. Space Science*, 54, 497
- Buote, D.A., Humphrey, P.J. 2012, *Astrophysics ans Space Science Library*, 378, 235
- Canuto, V., Adams, P. J., Hsieh, S.-H., & Tsiang, E. 1977, *PhRvD*, 16, 1643
- Cappellari, M., Scott, N., Alatalo, K. et al. 2013, *MNRAS*, 432, 1709
- Carroll, S. M., Press, W. H., & Turner, E. L. 1992, *ARA&A*, 30, 499
- Cervero, J., Estevez, P.G. 1982, *Nuovo Cimento*, 67B, 202
- den Heijer, M., Oosterloo, T.A., Serra, P. et al. 205, *Astron. Astrophys.* 581, A98
- de Swart, J.G., Bertone, G., Hooper, D. *Nature Astronomy*, 1,
- Dirac, P. A. M. 1973, *Proceedings of the Royal Society of London Series A*, 333, 403
- Eddington, A. S. 1923, *The mathematical theory of relativity*, Chelsea Publ. Co. New York, 270 p.
- Faber, S. M. and Jackson, R. E. 1976, *ApJ*, 204, 668
- Frieman, J. A., Turner, M. S., & Huterer, D. 2008, *ARA&A*, 46, 38
- Genzel, R., Schreiber, N.M., Forster Schreiber, N.M., Ubler, H. 2017, *Nature*, 543, 397
- Katz, H., Lelli, F., McGaugh, S. et al. 2017, *MNRAS*, 466, 1648
- Lang, P., Forster Schreiber, N.M., Genzel, R. 2017, *ApJ*, 840, 92L
- Lelli, F., McGaugh, S.S., Schombert, J.M., 2016, *AJ*, 152, 157
- Lelli, F., McGaugh, S.S., Schombert, J.M., Pawlowski, M.S., 2017, *ApJ*, 836, 152
- Maeder, A. 2017a, *ApJ*, 834, 194
- Maeder, A. 2017b, *ApJ*, 847, 65
- Maeder, A. 2017c, *ApJ*, 849, 158
- Maeder, A., Bouvier, P. 1979, *Astron. Astrophys.*, 73, 82
- McGaugh, S.S., Schombert, J.M., Bothun, G.D. and de Blok, W. J. G. 2000, *ApJL*, 533, L99
- McGaugh, S.S., Lelli, F., Schombert, J.M. 2017, *Phys. Rev. Letters*, 117, 201101
- Milgrom, M. 1983, *ApJ*, 270, 365
- Milgrom, M. 2009, *ApJ*, 698, 1630
- Sancisi, R. 2004, *IAU Symp.* 220, *Dark Matter in Gakaxies*, ed. S. Ryder et al., p. 233
- Seabroke, G.M., Gilmore, G. 2007, *MNRAS*, 380, 1348
- Sofue, Y., Rubin, V. 2001, *ARA&A*, 39, 137
- Sohn, J., Geller , M. J., Zahid, H. J. et al. 2016, *ApJS*, 229, 20
- Spitzer, L., Schwarzschild, M. 1951, *ApJ*, 118, 106
- Strigari, L. E., Koushiappas, S. M., Bullock, J. S. 2008, *ApJ*, 678, 614
- Tully, R. B., Fisher, J.R. 1977, *Astron. Astrophys.*, 54, 661
- Weyl, H. 1923, *Raum, Zeit, Materie. Vorlesungen über allgemeine Relativitätstheorie*. Re-edited by Springer Verlag, Berlin, 1970
- Wolf, J., Marinez, G. D., Bullock, J. S. et al. 2010, *MNRAS*, 406, 1220
- Wuyts, S., Forster Schreiber, N.M., Wisnioski, E. 2016, *ApJ*, 831, 149